

Constraints on Europa's surface properties from primary and secondary crater morphology

E. B. Bierhaus¹ and P. M. Schenk²

Received 4 June 2009; revised 29 June 2010; accepted 6 September 2010; published 7 December 2010.

[1] We investigate the near-surface properties of Europa's ice shell by examining small crater morphology; we use both primary and secondary craters for our analysis. For primary craters, the simple-to-complex transition provides an estimate of 0.19–0.36 MPa for the cratering effective strength. Through the aggregate statistics of over 100 profiles, we find that secondary craters on Europa tend toward smaller depth-to-diameter (d/D) ratios than primary craters, consistent with observations on other cratered surfaces (the Moon and Mars). In addition, we find that adjacent secondaries tend to be more shallow than distant secondaries, also consistent with trends seen on the Moon and Mars. The presence of numerous and far-flung secondaries requires a solid, competent surface for spallation that is inconsistent with weak ice. Although the effective strength evaluated by crater scaling laws does not have a direct quantitative relationship to lab-based measurements of shear or tensile strength, comparison to other observationally derived effective strengths and geologic materials suggests that the mechanical properties of Europa's surface ice should be consistent with terrestrial measurements of cold ice.

Citation: Bierhaus, E. B., and P. M. Schenk (2010), Constraints on Europa's surface properties from primary and secondary crater morphology, *J. Geophys. Res.*, 115, E12004, doi:10.1029/2009JE003451.

1. Introduction

[2] Over a decade after Galileo first returned new images of Europa, the unusual surface of this icy moon of Jupiter continues to confound us. Europa expresses two main techniques of endogenic resurfacing: ridge and chaos formation. (Each has several different subcategories that we will not discuss.) Both have been the subject of intensive investigation, but despite the significant effort to understand these features, there is no model that yet can demonstrate unambiguously how they form. Part of the difficulty is the relatively unknown state of Europa's surface; although known to be almost pure water ice [Spencer, 1987] at about 100 K [Spencer *et al.*, 1999], there are uncertainties in the material properties, such as porosity and tensile and compressive strengths. Because ridge and chaos formation models require knowledge of these parameters, uncertainty has led to divergent results.

[3] In contrast, crater formation is a (relatively) understood process; decades of lab-scale impact experiments, past and ongoing advances in computations for the high-energy and high-pressure events, and observations of craters on surfaces throughout the solar system have led to a common set of scaling laws that are reasonably good at linking the impactor, target, and resulting crater morphology. There are notable exceptions (formation of features seen in complex craters, such as central pits, central peaks, or multiring

structures), but the scaling laws are good for correlating the formation of simple, bowl-shaped craters.

[4] Several researchers [Moore *et al.*, 1998; Moore *et al.*, 2001; Turtle and Pierazzo, 2001; Turtle and Ivanov, 2002; Schenk, 2002] have used the morphology of the few, large European primary craters to provide strong constraints on the bulk characteristics of the icy shell. We employ this technique, but focus on the morphology of small, simple primary craters and the morphologically previously unexplored secondary craters. Several impact parameters are known, or at least well constrained, for a secondary impact, e.g., impact angle (which, on an airless world such as Europa, is the same as the ejection angle of ~45 degrees), impactor speed (either known because distance between primary and secondary is known, or well constrained because the impact speed cannot be greater than Europa's escape velocity), and impactor type (a ballistic piece of Europa's surface). The small craters probe the surface and near-surface properties of the ice shell, i.e., that portion of the ice shell through which the enigmatic ridges and chaos express themselves.

[5] We use topography from shadow measurements, photogrammetry, stereo images, and stereo-controlled photogrammetry to measure aspects of crater morphology; in particular, we measure depth: diameter (d/D) ratios of small primaries and secondaries, as well as examine the transition between simple and complex craters. These characteristics are clues to the mechanical properties of Europa's surface over vertical scales of the crater depths, i.e., tens of meters to a few hundred meters.

[6] The remainder of the paper proceeds as follows: in section 2 we discuss existing constraints for Europa's ice shell; in section 3 we describe the topographic data and

¹Space Systems Company, Lockheed Martin, Denver, Colorado, USA.

²Lunar and Planetary Institute, Houston, Texas, USA.

uncertainties; in section 4 we review crater d/D trends and present our data for Europa; in section 5 we discuss how our observations provide constraints on Europa's near-surface properties; in section 6 we describe the ridge response to cratering and the possible additional constraints on surface properties; and in section 7 we summarize and conclude.

2. Existing Constraints on Europa's Surface Properties

[7] Europa's surface of nearly pure water ice is exotically familiar: at once invoking strong analogies to terrestrial polar environments, and likely composed of familiar ice Ih, but displaying the vast array of ridges and chaos that have been difficult to explain. Though not for lack of effort. Researchers have conducted considerable work, observational, theoretical, and experimental, to untangle the mysterious European features.

[8] *Spencer et al.* [1999] use Galileo photopolarimeter-radiometer (PPR) data to determine surface temperatures between 86 K and 132 K, with a mean surface temperature of 106 K. For that temperature and zero surface pressure, the expected state of Europa's surface is ice I [*Durham and Stern*, 2001], the same form of ice found on Earth's surface. The derived thermal inertia [*Spencer et al.*, 1999] is about 20 times lower than that of solid ice and thus indicates a particulate surface, though the PPR measurements probe only the top few cm, and cannot be extrapolated to greater depths. Radar observations, however, can penetrate to greater depths. *Black et al.* [2001b, 2001a] present 3.5 cm, 13 cm, and 70 cm radar observations, and model fits to the observations, of Callisto, Ganymede, and Europa. Best fit parameters to the observations indicate that Europa's near surface is strongly volume scattering; up to 80% of the scattering layer's volume may be occupied by the scattering, indicating a very porous upper layer. In this case the scattering layer is only a few meters thick; as the volume density of scatterers decreases, the scattering layer thickness increases. (Ganymede and Callisto have progressively less volume scattering.) The decrease in returned signal via scattering with increasing wavelength (indeed, there was not a definitive return signal for the 70 cm data) indicates a decrease in scatterers with increasing size.

[9] *Eluszkiewicz* [2004] demonstrates that void spaces with diameters up to one meter could remain uncompacted in the upper 100 m (and maybe even the upper 1000 m) for hundreds of millions of years, longer than the current-best-estimate surface age of 60 Myr [*Zahnle et al.*, 2003]. While the [*Black et al.*, 2001b] radar data may not probe to those depths, the *Eluszkiewicz* [2004] results nevertheless demonstrate Europa's crust could maintain a measure of porosity to depths that approach a significant fraction of the brittle-layer thickness (regardless of whether the brittle layer rests on top of warmer, more viscous ice or has direct contact with a liquid layer).

[10] Initial models of Europa's ridges in general, and cycloid features in particular, assumed that they formed in tension from the diurnal tides [*Hoppa et al.*, 2001]. For their models to match the observations, they require crack initiation strengths (e.g., the tensile strength necessary to open a crack) of 25–50 kPa. While that tensile strength is lower than that of laboratory measurements (~1.2 MPa at –10 C

[*Schulson*, 1999]), their models provide good agreement with the observations. The inconsistency between the model-required strength and lab measurements, especially when considering ice strength increases with decreasing temperature [*Arakawa and Maeno*, 1997; *Stewart and Ahrens*, 2005], has been a puzzle.

[11] The two basic hypotheses for Europa's ice shell are that (1) it consists of an entirely brittle layer or (2) a brittle layer on top of a ductile layer. On the basis of the observations summarized above, the brittle layer, regardless of the presence or absence of a ductile layer, could possess and maintain a porous structure of at least 100 m depth for a duration greater than the estimated surface age. While early models of ridge production favored formation under tension and required low tensile strength, subsequent work [*Michalski and Greeley*, 2002; *Sarid et al.*, 2002; *Spaun et al.*, 2003] suggests that compression and shear are also at play, though currently those models do not provide improved constraints on the mechanical characteristics of the shell.

3. Measurement Description

[12] We used photogrammetry, stereo data, shadow measurements, and stereo-controlled photogrammetry to measure the d/D value for simple primary craters and for secondary craters.

3.1. Stereogrammetry

[13] The two major techniques for topographic mapping used here have been described elsewhere [*Schenk*, 2002; *Schenk and Pappalardo*, 2004]. Stereogrammetry involves the analysis of semicontrolled stereo images using computer algorithms. Once image registration is complete, this process is largely automated, using scene recognition algorithms to measure parallax, from which heights are calculated using vector algebra. Although the density of topographic (and corresponding intensity) information is very high in most Europa images and results in very clean DEMs, occasionally the scene matcher reports a spurious point, resulting in a spurious elevation value. These points are easily recognized as noise and can be removed through a variety of digital filters. Stereo coverage of Europa is limited to roughly 24 sites based on stereo image mosaics of one to six images across (30–100 km across). Scene recognition uses discrete patches (3×3 – 5×5) in each image to make the stereo match, degrading DEM resolution by a similar factor relative to the resolution of the lowest-resolution image in the stereo pair. The primary source of error in stereogrammetry is associated with the lack of a global elevation database to reference the stereo DEM to. Although every effort was made to register stereo images as precisely as possible, some uncertainty in the tilt of the DEM remains, but these errors are uniform across the stereo scene and will not alter the measured d/D . Limb profiles of Europa confirm there are few or no steep regional gradients.

3.2. Photogrammetry

[14] Shape-from-shading (photogrammetry or PC) involves estimating surface slopes in monoscopic images or mosaics taken at low Sun (incidence angles of greater than 65°), from which a regional topographic model can be derived. While more advanced versions of this technique are possi-

ble, the severe data rate restrictions of the Galileo mission did not permit the type of overlapping imaging required. The technique applied here [Schenk, 2002, 2009] uses a photometric function [e.g., McEwen, 1990] to estimate surface slopes, based on a set of assumptions. Unlike stereogrammetry, these maps are not controlled by the image plane, and residual errors can build up across the scene. These errors tend to be quite small at pixel scales (less than a few percent), but can accumulate over longer distances of tens to hundreds of pixels. This can result in warping of the DEM, the presence or magnitude of which can be essentially unconstrained without corroborating information. The nature and potential magnitude of these errors are discussed in the next section.

3.3. Combined (Controlled) DEMS

[15] We are fortunate on Europa that images were targeted in such a way that most stereo and PC-DEMs are coincident and can be used to mitigate the deficits of each method. The stereo DEMs are too low in resolution to use for most craters of interest here, while the PC-DEMs have inherent longer wavelength uncertainties and possible local scale anomalies (see below). In these cases, the stereo DEM can be used to control the long wavelength, incorporating the high spatial frequency of the PC data with the long wavelength stability of the stereogrammetry. Stereo-controlled PC DEMs constitute the majority of our data (except where noted).

3.4. Sources of Error

[16] Our data rely primarily on the PC component of the DEMs, due to our interest in small-scale features. With the exception of the E15ETTYRE site, most if not all secondaries are not resolved in the stereogrammetry DEMs, due to the resolution of the weaker stereo images and the significant patch size (3×3 – 5×5) used by the automatcher. Hence, our error analysis focused on the PC artifacts.

[17] Although other errors occur [Jankowski and Squyres, 1991; Efford, 1991], stereo control in most of our examples mitigates most of these. The primary source of error remaining in our analysis is knowledge of the photometric function of the surface on both regional and pixel scales. The regional photometry of the terrain on which these craters formed is governed by the normal albedo a and the phase function L . These parameters are estimated using global images and fits to the brightness changes across them [e.g., McEwen, 1986]. Once an estimate of L is made [Schenk, 2009], then the normal albedo of the terrain in the scene is estimated using a best fit approach such that the residuals between the model brightness and actual brightness across the scene is minimized. Despite the small scale of most of our images (typically 30–100 km across), there are regional albedo gradients that can occur across or within scenes. Using a best fit approach may result in albedos that are too low or too high for a given parcel of terrain, resulting in slope estimates that are also too high or too low. This effect, where it occurs, can be mitigated by two means. The first is our use of low-phase images to model the albedo variations across Europa, as described above. The second is stereo control, which removes these residual regional gradients from the PC-DEM, thereby correcting slope estimates.

[18] Pixel-scale albedo variations are more pernicious. Careful examination of Galileo high-resolution images

reveals the presence of small bright and dark spots a few pixels across or less on the inner rim slopes and floors of some but not all impact craters. Indeed, such deposits are not uncommon on the flanks of or the valleys between some ridges. The origins of these spots are unknown (and important in their own right) but are not resolved in the local albedo models used in our PC technique due to the lower resolution of the low-phase angle images used. Hence, the PC technique will model these deposits as anomalously low or high slopes. Although we restrict measurements to craters no smaller than 5 pixels across to limit resolution effects, local albedo effects can be important in some cases. We make an effort to quantify these errors.

3.5. Variation in L

[19] The photometric function used here is the combined lunar-Lambertian function described by McEwen [1991]. Here L describes the fraction contribution of the lunar and Lambertian components. The value of L for individual terrains is not known but a mean value can be estimated for Europa [Schenk, 2009] and is dependent on phase angle. This value is uncertain to $\sim 10\%$ in the phase angle range for which we have data. Figure 1 shows the functional dependency of the measured d/D ratio on L for a ~ 600 m primary crater. The variation of d/D due to L is not sufficient to explain the variation of d/D we see in the observations, thus we believe we are measuring real variations in the crater profiles. Figure 1 shows the functional dependency of the measured d/D ratio on L for a ~ 600 m primary crater.

3.6. Variation in a

[20] The value of a , the normal albedo used in the photometric function, is also not well known for individual terrains on Europa. Instead, a mean value can be estimated for each map, or a low-resolution local albedo map can be used as described above. The bright features we observe are typically only a fraction of the crater diameter but may play a role in our measurements. Without high-resolution albedo maps, their importance is difficult to quantify. The value of a is typically uncertain to $\sim 5\%$ for any given scene, but at local scales can be more variable. Figure 2 shows the functional dependency of the measured d/D ratio on a for the same crater as in Figure 1.

3.7. Asymmetric Profiles

[21] When surveying the compiled data sets, we observed a tendency for craters to appear asymmetric (high on the sunlight side) in many but not all cases. Europa is pervasively ridged on kilometer scales [e.g., Figueredo and Greeley, 2004] and asymmetric profiles are to be expected in many if not most cases as kilometer-scale craters will reflect underlying topography. It is likely that many of these profiles are real, given the topography, but the preference for sunlight sides suggests a possible bias relating to the small bright spots seen on some crater floors. To mitigate against any bias, we report here only measurements from the craters wall facing away from the Sun.

3.8. Shadow Lengths

[22] Using stereo to control the PC data mitigates most of the errors inherent in PC data, but does not eliminate them completely. The most likely sources of error here are

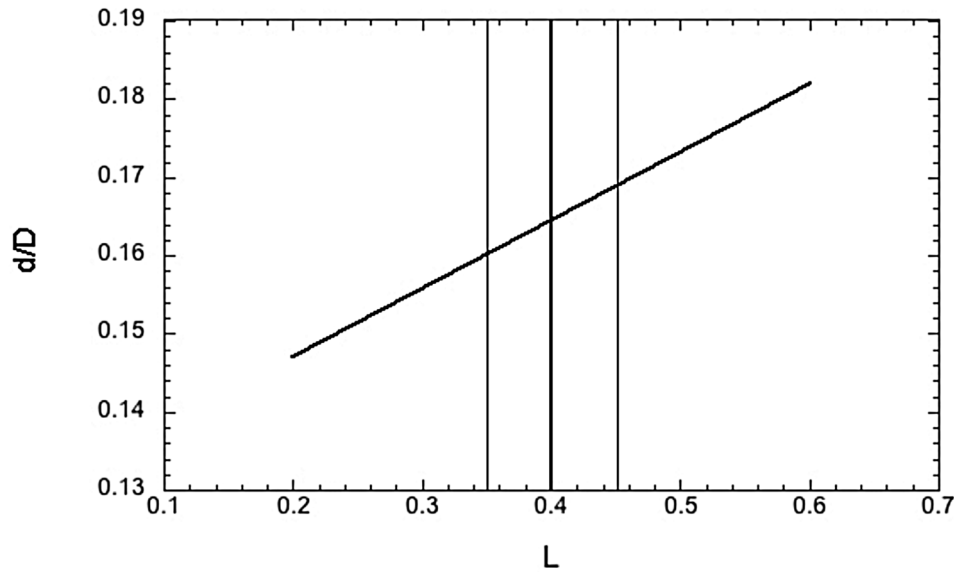


Figure 1. Plot of measured crater d/D as a function of photometric parameter L for a 600 m crater on Europa near Thrace Macula. Data are from photoclinometry. The diagonal line is the d/D estimate as a function of L . The heavy vertical line is the estimated L value for this observation; the thin lines are the plausible range of values for L .

the small pixel-scale variations in local albedo that can occur on local slopes. As a test of the reliability of our data, we obtained a set of shadow length measurements at the three of our sites where shadows are ideally situated at the bottom-most point in craters to provide maximum crater depths. These are the E17STRSLP01, E17AGENOR03, E17THYLIN01 sites. These are the d/D values shown in Figure 3 with error bars. The errors shown assign a 1 pixel error in measuring the edges of the shadow, and because of

the accuracy that these edges can be measured, we limit ourselves to the largest craters, i.e., those greater than about 7 pixels across on the image plane. The shadow length depth measurements all fall within the data cloud measured from the high-resolution DEMs. This ensures that although any one profile from the PC data may be noisy, the aggregate trend of numerous profiles provides a meaningful constraint on the true d/D of craters near the resolution limit.

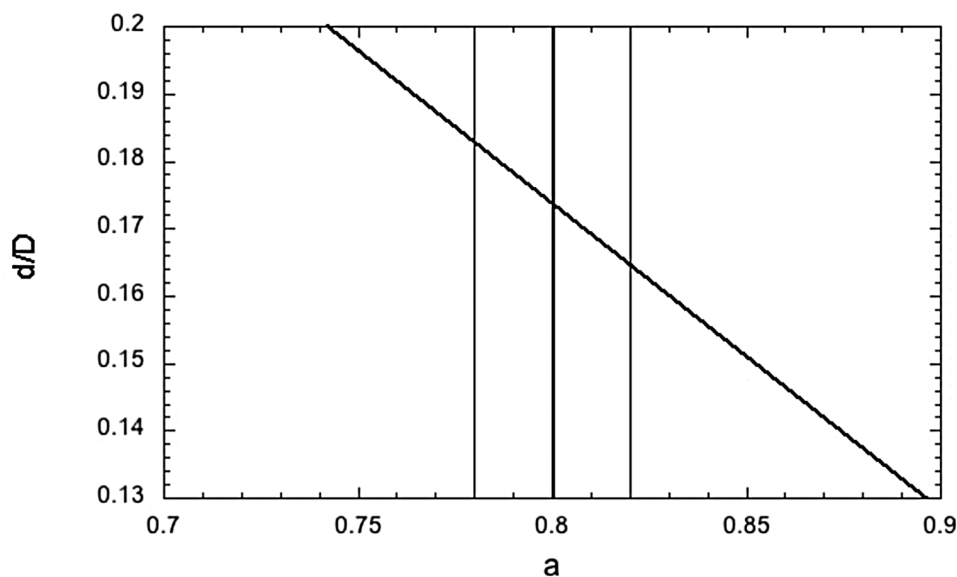


Figure 2. Plot of measured crater d/D as a function of photometric normal albedo a , for a 600 m crater on Europa near Thrace Macula. Data are from photoclinometry. The heavy vertical line is the estimated a value for this observation, the thin lines are the plausible range of values for a .

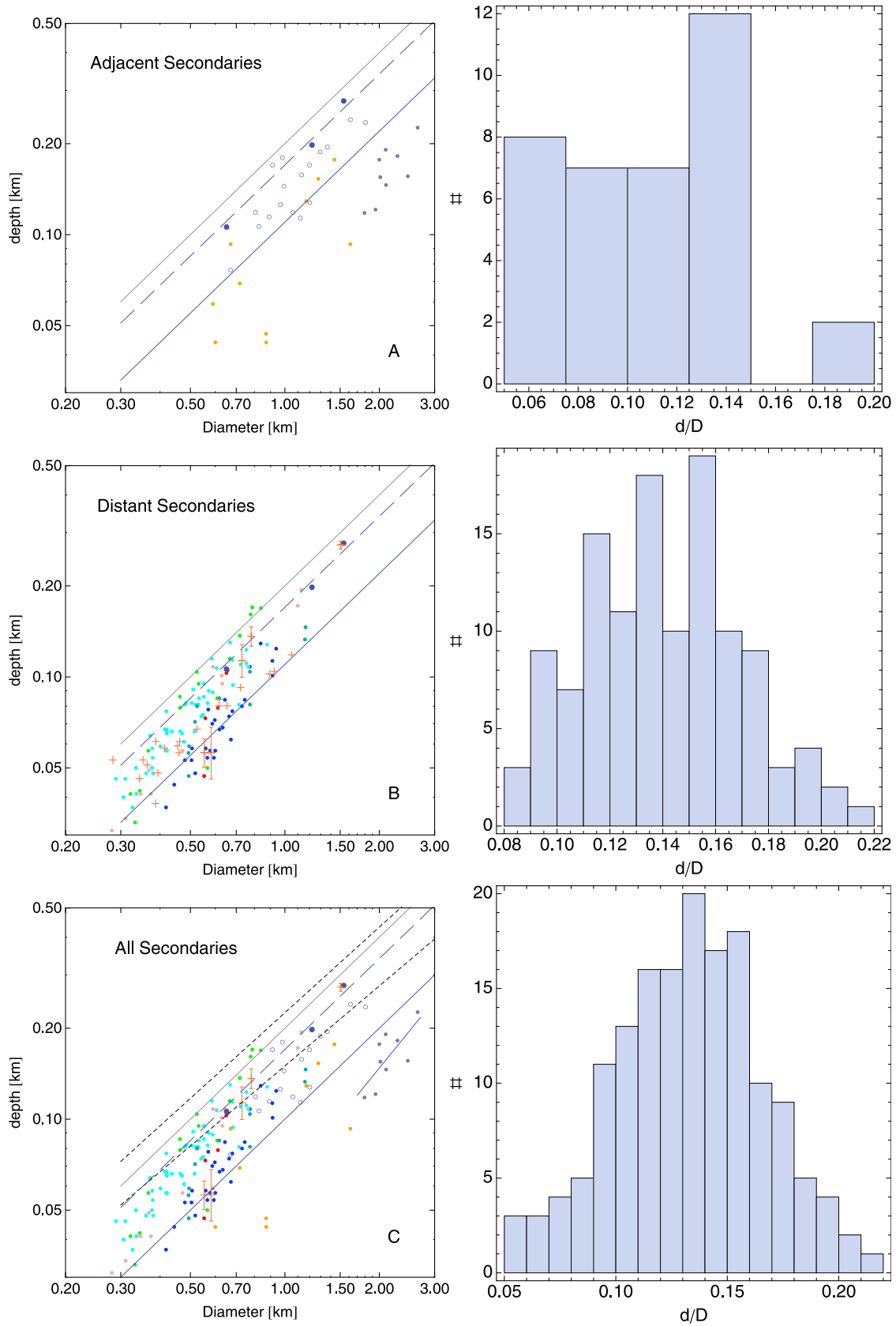


Figure 3

[23] The scatter in the shadow data are indicative of the variability inherent in such data. There are several sources for such scatter, the prime of these are natural variations in crater shape (even Meteor Crater does not have a uniformly high rim crest) and, as indicated above, the uneven nature of the original surface. The surface geology of Europa is exceedingly complex and most craters form on slopes, such as ridge flanks, tilted blocks or rolling plains, or on the faults or fractures that are pervasive across Europa. Rim crests in these craters will have topography that reflect these original slopes and flaws, and as shadows are single point measurements will reflect some scatter to lower or higher depths depending on the orientation of the original slope. To reduce this source of scatter, we avoided most (but not all) shadowed craters in the rugged ridged plains regions. It is clear however, that the shadow measurements support the general validity of the more extensive data set.

4. Crater Depth-to-Diameter

4.1. Primary Crater Depth-to-Diameter

[24] Crater depth-to-diameter ratios have long been a fundamental means to compare craters on a single object, and between planetary surfaces. *Pike* [1980] provides data for the d/D values and the transition diameters (from simple to complex) for craters on the Moon, Mars, and Earth. For fresh, simple craters on all of the surfaces, the d/D is ~ 0.2 . The transition diameter clearly follows a $1/g$ relation (where g is surface gravity), i.e., complex craters appear at smaller diameters for surfaces with higher gravity; however, material properties of the surface also play some role in establishing when complex features appear. For all three planets, the transition occurs at smaller diameters for weaker surfaces (sedimentary rock on Earth, fractured highlands on the Moon, and icy soils on Mars) than on stronger surfaces (crystalline rock on Earth, the volcanic mare on the Moon, and the rocky highlands of Mars). Figure 3 of *Pike* [1980] clearly demonstrates that while gravity is the dominant factor for transition diameter, material properties contribute as well.

[25] Craters on icy surfaces follow a similar progression in morphology to that demonstrated by their rocky cousins, except that the transition diameters (e.g., from simple to complex) are shifted to lower diameters for the icy bodies as a group [*Chapman and McKinnon*, 1986; *Schenk*, 1991, 2002]. Simple primary craters on icy surfaces for which we have reliable measurements, including Enceladus, Ganymede, and Callisto, have d/D shape ratios (~ 0.2) similar to those on rocky surfaces [e.g., *Pike*, 1977].

[26] The lone exception may be Europa. Galileo-based measurements of simple primary craters indicate d/D ratios of ~ 0.17 [*Schenk*, 2002; *Schenk et al.*, 2004]; and some

measurements in this paper, see Figure 3], with some craters as deep as 0.2. The uncertainties prevent absolute distinction between the values of 0.17 and 0.20, but the nominal d/D value for most simple primaries on Europa is systematically less than 0.2, and is best fit by 0.17. The reason for this discrepancy is unknown, and may be attributable to measurement uncertainty. Error in the global control network is possible but not very likely and difficult to test with current imaging data. It is possible that a thin regolith may change the inherent shape of simple craters, but no difference has been identified in lunar craters on mare and highlands, and the only craters on as similarly young icy surface for which we have data, Enceladus, have ratios of 0.2 (*P. Schenk*, personal communication, 2009). These data [*Schenk*, 2002; *Schenk and Bussey*, 2004] were derived from shadow length measurements and are not subject to the errors associated with PC. We emphasize that while the mean of 0.17 is far from conclusive, it is suggestive.

4.2. Secondary Crater Depth-to-Diameter

[27] Secondary craters tend to have a more shallow d/D than primary craters, but there may be more than one physical process that contributes to the difference. *Oberbeck and Morrison's* [1973] experiments and observations of secondary clusters (close to their parent primary) demonstrate that ejecta curtains from neighboring secondary craters, which formed simultaneously, can create a distinct ridge between the craters; the ejecta from the near-simultaneous formation of several such craters leads to the herringbone pattern, and can create infilling of neighboring craters. *Schultz and Gault's* [1985] experiments of clustered impacts demonstrate that closely spaced impactors lead to shallow craters. *Pike and Wilhelms* [1978] analyze 150 lunar secondary craters, ranging in size from 200 m to 43 km. They based their identification of secondary origin on clustering, mutual interference features, and correlation with parent primary. (The largest secondaries are from either Imbrium, Orientale, or Serenitatis basins.) While they found that secondaries exhibit the same progression of morphology with size (flat floors, central peaks, and perhaps rimwall terraces), these transitions took place at larger diameters than for the progression seen in primary craters. All secondaries demonstrate a shallow d/D , with an average of 0.11; however, they found a trend of increasing d/D with increasing range from parent primary. For a scaled range of the secondary by the primary radius (R_s/r_p), they found at $R_s/r_p = 3.0$, the d/D is 0.09; at $R_s/r_p = 7.0$, the d/D is about 0.12; and at $R_s/r_p = 35.0$, d/D is 0.14.

[28] Comparing d/D values between adjacent and distant secondary craters suggests that impact velocity, and the corresponding induced peak pressure in both the target and

Figure 3. The d/D values for 154 European secondary craters and three small primary craters: the different colors represent measurements from different regions and the three large blue points in each of the plots are the small European primaries seen in Figures 9a–9c. (a) The d/D for adjacent secondaries around Tyre and Callanish. The open circles are Tyre stereo measurements, the closed gray circles are Tyre PC measurements, and the orange circles are Callanish PC measurements. The dashed blue line is for $d/D = 0.17$, the solid black line is for $d/D = 0.2$, and the solid blue line is for $d/D = 0.10$. (b) The d/D for distant secondary craters from six regions; the lines are as in Figure 3a. (c) The d/D for all measured secondary craters. The two dashed black lines are the [*Pike*, 1977] best fits for simple lunar craters, $d = 0.15D^{0.88}$ (lower line) and $d = 0.225D^{0.941}$ (upper line). The solid blue line segment is the best fit $d = 0.061D^{1.276}$ for the Tyre PC data.

impactor, plays a significant role in determining the final crater morphology. Impact experiments into ice, such as those by *Kato et al.* [1995], indicate morphological transitions with impact velocity. Even the distant and more dispersed secondaries express a shallow d/D relative to primary craters (though the d/D increases with increasing distance from the primary crater).

[29] Using photogrammetry, stereo, and some shadow lengths, we measured the d/D of 154 secondary craters seen in Galileo images. The measurements fall into two categories:

[30] 1. Adjacent secondaries, or those that appear within a few crater radii of their parent crater. The only adjacent secondaries sufficiently resolved to measure d/D are those around the multiring impact structures of Tyre and Callanish. We obtained the Tyre measurements from ~ 170 m/pix photogrammetry images, and ~ 40 m/pix stereo images.

[31] 2. Distant secondaries, those that are far from their parent crater. Measurements in this category are from photogrammetry and shadow lengths.

[32] Degradation effects, which could significantly change the d/D values between the time of formation and the time of the Galileo image acquisition, should be minimal. There is no atmosphere to create aeolian deposits, as on Mars, and the average surface age is very young compared with both Mars and the Moon, minimizing the effects of impact gardening at the scales of hundreds of meters. Topographic degradation of any landform on Europa seems to occur at two different rates: a slower (but potentially still relatively rapid on geologic time scales given Europa's overall youth) disaggregation in chaos regions, and a more rapid and thorough reconstruction of the surface by ridge formation. Europa's larger craters are all relatively pristine [*Moore et al.*, 2001; *Bierhaus et al.*, 2009; *Schenk and Turtle*, 2009], and downslope movement seems restricted to very steep slopes (e.g., cliffs) that are not present in secondaries. Thus, we believe the measurements reflect the values that existed at the time of crater formation.

[33] Figures 3a–3c plot the d/D measurements and their histograms. Each d/D plot also contains the d/D value for the three small primaries seen in Figure 9, represented by the three filled blue circles. The first plot is for adjacent secondaries around Tyre and Callanish: the open circles are stereo measurements near Tyre, the filled gray circles are PC measurements around Tyre, and the orange circles are PC measurements around Callanish. The solid black line is for $d/D = 0.2$ (the trend for simple primary craters on most cratered surfaces), the dashed blue line is for $d/D = 0.17$ (the trend for simple primary craters on Europa, *Schenk* [2002], and well matched by the three small primaries in this plot), and the solid blue line is for $d/D = 0.10$ (a “representative” trend for secondaries). There is a spread of values over the measured diameter range due to the uncertainty and noise in the profiles, but almost all are below $d/D = 0.17$, and some are much more shallow.

[34] The second plot is for distant secondaries seen in six regions. The data with error bars are shadow measurements; the error bars assume a one pixel error on the measurement. The shadow measurements and the error bars fall within the scatter of the other data, which supports the reliability of the other measurements. The trend lines are the same as in the first plot. Here too there is scatter at any given diameter, however the bulk of the measurements fall between $0.1 \leq$

$d/D \leq 0.17$. It is likely the greater spread of the distant secondaries results from the sampling of a wider range of ejection, and thus impact velocities. This results in a range of peak pressures, which we discuss in more detail below.

[35] The third plot combines all measurements, as well as adding three new trend lines. The two dashed black lines are the [*Pike*, 1977] best fits for simple lunar craters, $d = 0.15D^{0.88}$ (lower line) and $d = 0.225D^{0.941}$ (upper line). The first fit is for the thirteen smallest craters in his data set; although he does not specify that these are secondaries, the possible statistical dominance of secondaries over primaries at small diameters [*Bierhaus et al.*, 2005; *McEwen and Bierhaus*, 2006] could mean that the shallower fit was made to secondary craters. The solid blue line segment is the best fit $d = 0.061D^{1.276}$ for the Tyre PC data.

[36] In general, European secondaries are more shallow than simple primary craters, a trait seen on other cratered surfaces. Further, distant secondaries demonstrate a deeper average d/D value than adjacent secondaries. While no reliable data yet exist on the minimum speed to create a secondary crater, they can appear just beyond the continuous ejecta blanket of a primary crater, suggesting they form at speeds as low as a few hundred m/s. Their maximum impact speed is set by the escape velocity of the target object, which for Europa is about 2 km/s. (In general, fragments ejected at still higher velocities may yet be swept up by the parent object, or escape entirely and eventually hit another planet or satellite – for example, the lunar meteorites found on Earth. *Zahnle et al.* [2008] call those sesquinarities; we will not discuss those impactors here.) Given an upper limit of 2 km/s impact speed for ejecta fragments, the average primary impact speed on Europa, about 26 km/s *Zahnle et al.* [1998], is 13 times the maximum secondary impact speed.

[37] As presented by *Gault and Heitowitz* [1963], and summarized and reviewed by *Melosh* [1989], one can estimate the peak impact pressure as:

$$P_{\max} = \frac{\rho_o v_i}{2} \left(C + \frac{S v_i}{2} \right), \quad (1)$$

where P_{\max} is the peak pressure, ρ_o is the initial target density, v_i the impact velocity, and both S and C are parameters of the equation of state. This equation also assumes the impactor and target are compositionally identical (roughly appropriate for secondary impactors, but not necessarily correct for primary impactors). Figure 4a plots this equation for $200 \leq v_i \leq 2000$ m/s, and with values for C and S that are a function of impact velocity from *Stewart and Ahrens* [2005]. The peak pressure varies from about 300 MPa to about 2.5 GPa. While seemingly large, these values are still orders of magnitude smaller than the estimated peak pressure (nearly 250 GPa) for a primary impact; Figure 4b plots the ratio of the peak pressure of a secondary impact to that of a primary impact with $v_i = 26$ km/s. The plot indicates the somewhat arbitrary distinction between “near-field” and “far-field” secondaries. Near-field is for $v_i < 495$ m/s, or about 10 crater radii for Tyre, which is the largest primary impact crater (thus far identified) on Europa. Far-field is somewhat more quantified: *Stewart and Ahrens* [2005, Figure 5] show that at pressures around 1.25 GPa, ice at 100 K experiences significant volumetric changes not seen at smaller pressures;

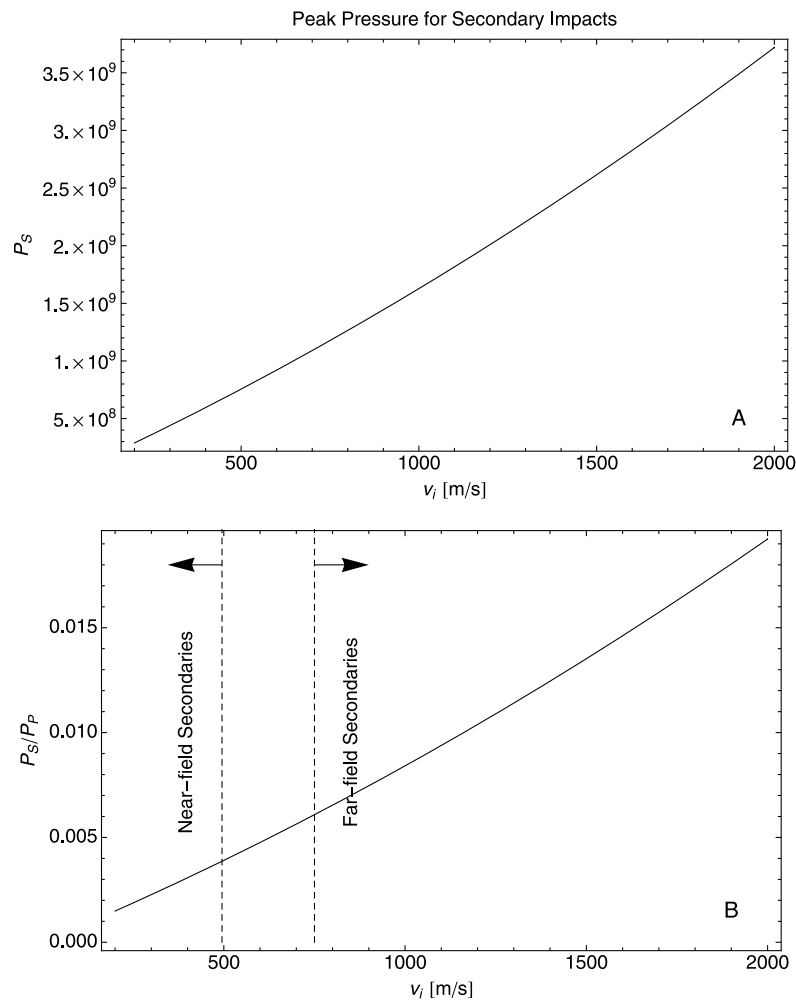


Figure 4. The estimated peak pressures for secondary impacts on Europa. (a) Estimated peak pressure for impact (and therefore ejection) velocities between 200 and 2000 m/s. The lower-velocity limit comes from observations of secondaries around the 15.5 km Rhiannon (the smallest secondary-producing primary observed at moderate resolution), whereas the upper-velocity limit is the approximate escape velocity. (b) The solid black line is the ratio of secondary-to-primary peak impact pressures as a function of secondary impact velocity. The maximum peak pressure for an ~ 2 km/s secondary impact is less than 2% that of a primary impactor of equivalent size. The ratio assumes a constant 26 km/s velocity [Zahnle *et al.*, 2003] for primary impactors; see text for further details. The dashed lines are approximate transitions between near-field and far-field secondaries. “Near-field” is somewhat arbitrarily defined as ejection velocity < 495 m/s, which corresponds to a range of about 200 km, or about 10 crater radii for the largest known crater on Europa (Tyre). “Far-field” is defined as ejection velocity > 750 m/s, which corresponds to a range of roughly 500 km between ejection and impact locations. Further modeling and experimentation could potentially clarify transitions in secondary crater morphology as a function of the peak pressure.

within the precision of our discussion, this corresponds to the velocity of 750 m/s.

[38] Because of the significant differences in the peak pressures of primary and secondary impacts, it is not unreasonable to expect morphological differences between the two. Distant secondaries form from fragments that have tens of minutes of flight time, a sufficient duration that even small “lateral” velocities spread the fragments into individual pieces. Because even distant secondary craters express shallow d/D values relative to primaries, it seems that the key contributor to secondary morphology is the lower-impact

velocities, which lead to lower peak pressures in both the target and projectile, which in turn dictate the nature of the excavation flow.

5. Using Crater Morphology to Estimate Strength

5.1. Strength Versus Gravity; Simple Versus Complex

[39] Typical discussions of late-stage crater formation and evolution distinguish between whether a crater formed in the strength regime or gravity regime. A crater forms in the strength regime when the target surface strength halts the

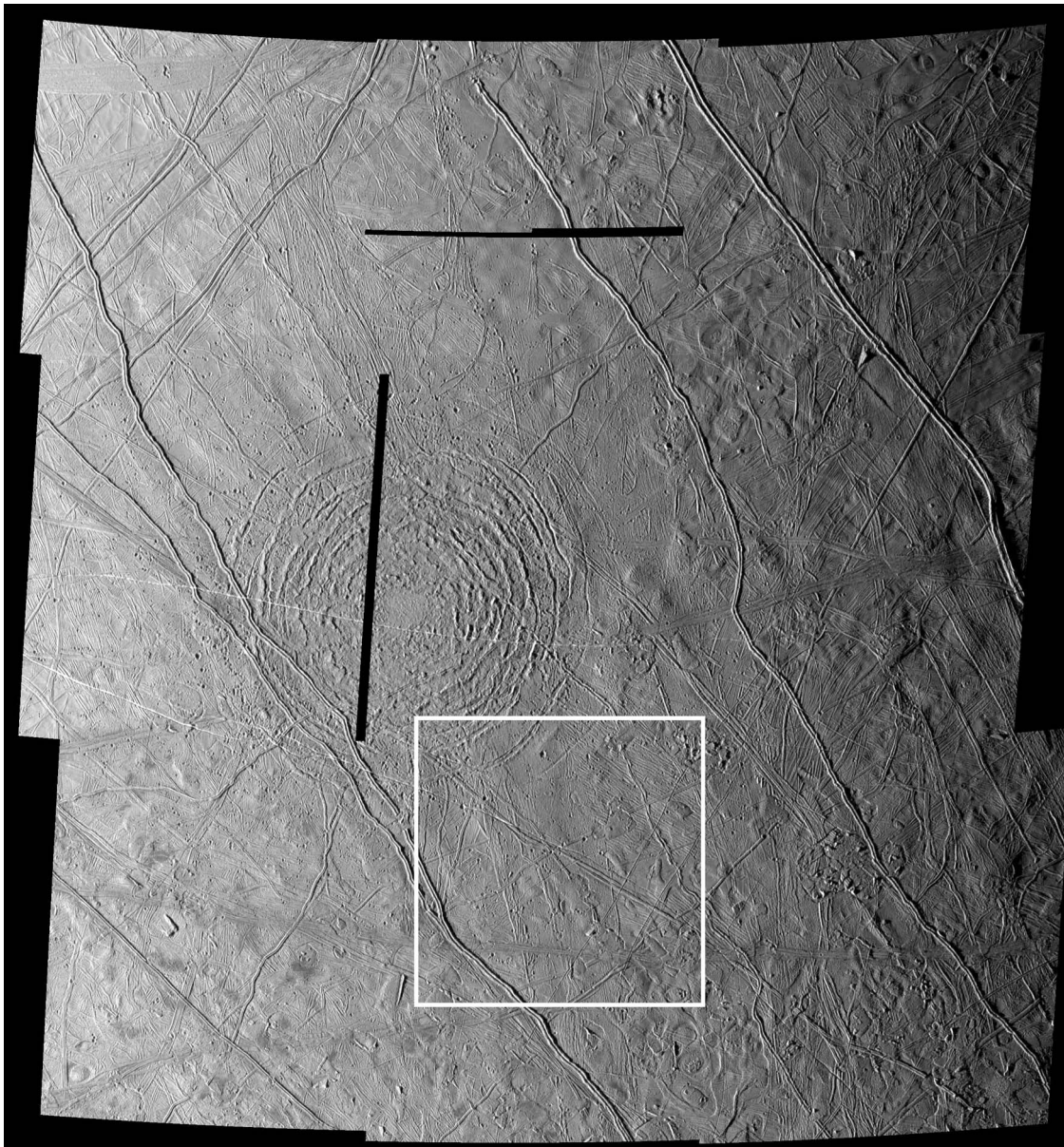


Figure 5. The Tyre multiring impact structure as seen in the Galileo E14TYREHR01 mosaic. The Sun is from the left, and the black bars are data gaps. The white box is the region shown in Figure 6. For scale, the edges of the white box are ~ 115 km in length.

formation of the crater; conversely, when surface gravity halts the growth of the transient crater cavity, the crater forms in the “gravity regime”. The handoff between the two regimes is known as the strength-to-gravity (StG) transition. As crater diameter increases, a second transition occurs, the simple-to-complex (StC) transition. For example, on the Moon the StG transition is expected to occur at a few hundred meters diameter, while the StC transition begins around 15 km [Pike, 1980]. The StC transition reflects when craters reach a sufficient diameter that the simple, bowl-shaped morphology evolves to more complex shapes, such as terraced rims and central peaks or pits.

[40] Identifying the StG transition diameter would seem a valuable means to estimate a surface effective strength. *Chapman and McKinnon* [1986] derive the transition to be:

$$D_{StG} \propto \bar{Y} g^{-1} \rho_p^{-\gamma} \rho_t^{\gamma-1}, \quad (2)$$

where \bar{Y} is an effective strength (see below), g is surface gravity, γ is a constant whose value is probably 2/3, and ρ_p and ρ_t are the projectile and target surface densities, respectively. *Chapman and McKinnon* [1986] plot an estimate of D_{StG} as a function of g for icy objects, but the value for Europa, with $g = 1.3 \text{ m/s}^2$, falls above the diameter of the simple-to-complex transition. Currently the StG transition is

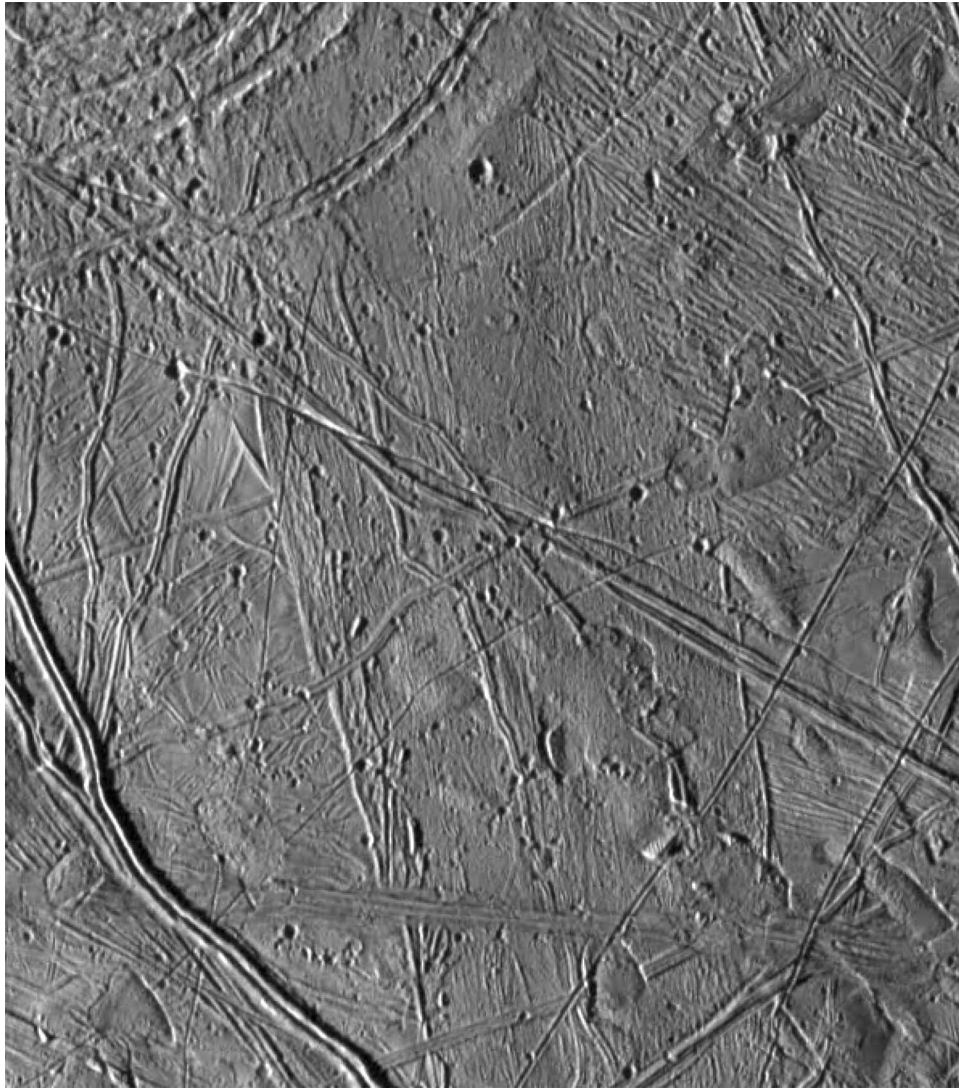


Figure 6. A portion of Tyre's adjacent secondary crater population. Several of these craters exceed 2 km diameter (see Figure 5) and so are gravity-dominated craters.

not well defined, and distinct morphological signatures are not known for the transition.

[41] Fortunately, however, there are obvious morphological signatures for the StC transition. The StC transition takes place when:

$$\bar{Y} = c\rho_tgh, \quad (3)$$

where h is the transient crater depth (distinct from the final crater depth that we measure), and c is a dimensionless coefficient with value <1 . To relate to crater diameter, assume that the transient depth is 1/4 of the transient diameter (e.g., $h = D_{tr}/4$, *Melosh* [1989]):

$$\bar{Y} = \frac{c}{4}\rho_tgD_{tr}. \quad (4)$$

For the StC transition, *Melosh* [1989] estimates that $\bar{Y} < 0.36\rho gh$, or $\bar{Y} < 0.09\rho gD_{tr}$ (for $h = D_{tr}/4$); *O'Keefe and Ahrens* [1993] estimate that $\bar{Y} = 0.11\rho gD$.

[42] Before we use this relation to estimate an effective strength, a word of caution on the physical interpretation of this value: As many authors [see, e.g., *Housen and Holsapple*, 2003; *Holsapple and Housen*, 2007; *Richardson et al.*, 2007; *Senft and Stewart*, 2007] describe, the physical interpretation of \bar{Y} is ambiguous. Geological materials, such as ice, exhibit different magnitudes for compressive, tensile, and shear strengths. Furthermore, any given strength can be a function of temperature, strain rate, ambient pressure, porosity, and grain size. During crater formation, initial pressure waves introduce compression and shear into the target, followed by a rarefaction wave in tension, which means that the target surface suffers compression, shear, and tension. The enormous kinetic energy of a planetary impact leads to very high pressures and temperatures at the impact site. The excavation flow that forms the crater occurs after the initial pressure wave(s) passed through and fractured the target material [*Nolan et al.*, 1996], so any lab measurements of material strength may not represent the target strength faced by the forces forming the crater. Prior to an impact, planetary crusts

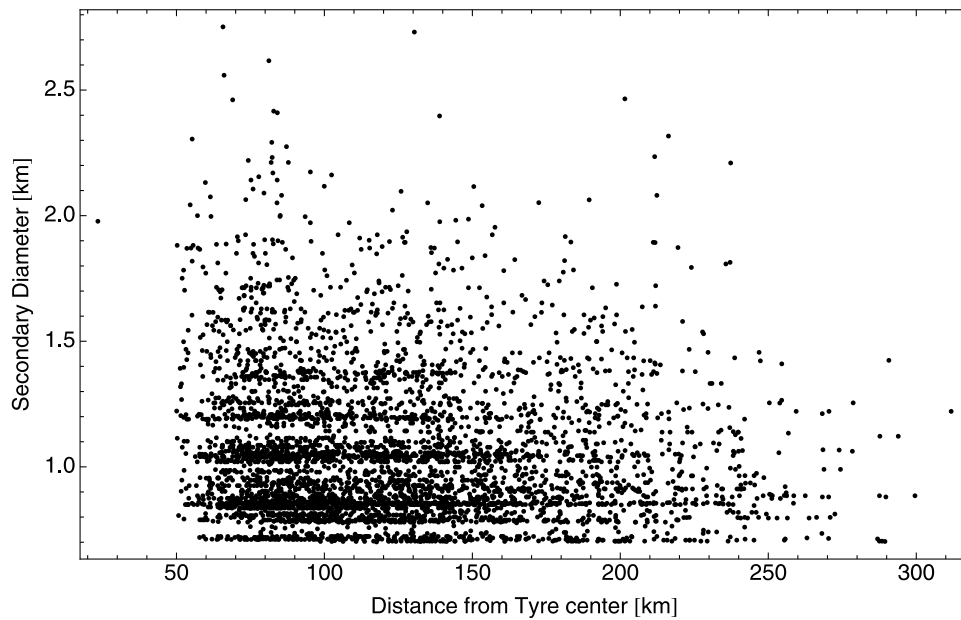


Figure 7. A plot of Tyre near-field (adjacent) secondary crater diameter as a function of distance from Tyre center. The data were measured from the Galileo E14TYREHR01 sequence, seen in Figure 5. The maximum diameter clearly decreases with increasing distance; the largest and most distant secondary visible in this sequence is ~ 1.2 km. The apparent quantization of secondary diameter values reflects that the original measurements were in discrete pixels; the quantization is somewhat smeared because of the slightly varying resolution between images within the mosaic (5 pixels in one image does not have the same km value as 5 pixels in another image).

can be a collection of faults, joints, fractures, and slopes, which lead to a different bulk strength than a small lab specimen of the same material. As a result, most researchers invoke the term “effective strength” as a generalized means to parameterize the target’s strength in response to crater formation. We appeal to the same convention here.

5.2. Using Primary Craters to Estimate Strength

[43] Using the simple but instructive formulation of equation (4), we can estimate Europa’s effective strength by using the observed 2–4 km [Schenk, 2002] transition diameter between simple and complex craters. Because the measured diameter is not the transient diameter, we first estimate the transient diameter using the [McKinnon and Schenk, 1995] relationship between the final (observed) crater diameter and transient diameter:

$$D = 1.176D_{tr}^{1.108}. \quad (5)$$

When we assign the minimum and maximum values of 2 and 4 km for the StC diameter, we obtain a transient crater diameter between 1.6 and 3 km.

[44] Combining the transient crater diameter with the European surface gravity of 1.3 m/s^2 , and an estimate surface density of 930 kg/m^3 , an average of the Melosh [1989] and O’Keefe and Ahrens [1993] versions of equation (4) ($\bar{Y} < 0.1\rho gD_{tr}$) estimates the corresponding effective strength to be between 0.19 and 0.36 MPa.

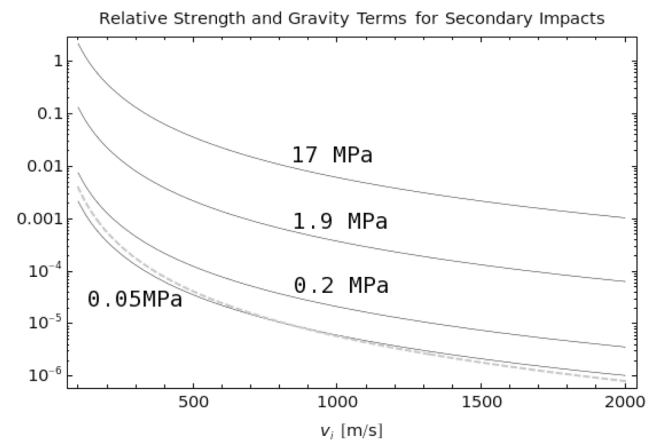


Figure 8. A plot of the relative magnitudes of the effective strength ($(\bar{Y} / (\rho_i v_i^2))^{2+\mu}$, black lines) and gravity term modified to reflect Tyre secondaries (gray line), as a function of impact velocity. The range of velocities reflects the approximate minimum and maximum impact velocities for ejecta fragments that make secondaries on Europa. The strengths plotted are 17 MPa [Lange and Ahrens, 1987], 1.9 MPa [Burchell et al., 2005], 0.2 MPa (this paper, approximate lower limit from the StC transition), and 0.05 MPa. The gray line assumes a 2 km impactor-formed Tyre. The largest Tyre secondaries form in the gravity regime, whereas the most distant may form in the strength regime. The approximate lower limit effective strength that permits this behavior is 0.05 MPa. There are no units for the vertical axis because both ratios are dimensionless.

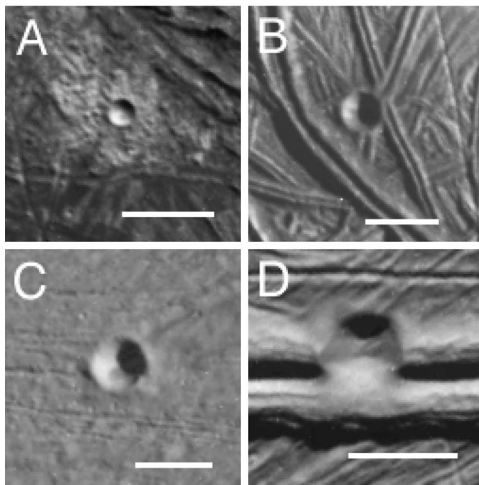


Figure 9. Four small craters that are likely primaries. (a) Galileo image sequence E17THRACE01: a 0.64 km, bowl-shaped crater in Thrace chaos with bright ejecta. (b) Galileo image sequence E17DISSTR01: a 1.3 km crater with a distinct rim; the profile of shadow along the crater floor indicates it is a “clean” bowl shape. At this resolution, there is no sign that the preexisting ridges controlled the growth of the crater rim or cavity. (c) Galileo image sequence E17AGENOR03: a 1.6 km bowl-shaped crater with subdued rim. (d) Galileo image sequence E17THYLIN01: a 1.5–1.8 km crater (depending on which diameter measured) that formed on a double ridge. The crater cavity appears to have formed by displacing ridge material. The scale bar in each image is 2 km.

5.3. Using Secondary Craters to Estimate Surface Properties

[45] The crater scaling laws use a point-source approximation [Holsapple, 1993], which requires that initial crater formation takes place in the strong shock regime. As just discussed, this may not be the case for adjacent secondaries, which form close to their parent primary. However, distant secondaries may form within this regime, which we assume for the following discussion.

[46] Holsapple [1993] reviews crater scaling laws and the impactor and target properties used to develop the scaling laws. The “cratering efficiency” compares the mass excavated from the crater with the mass of the impactor; from the scaling law it is possible to write an expression for the crater volume [see also Richardson *et al.*, 2007]:

$$V = K_1 \left(\frac{m_i}{\rho_t} \right) \left[\left(\frac{ga}{v_i^2} \right) \left(\frac{\rho_t}{\rho_i} \right)^{-\frac{1}{3}} + \left(\frac{\bar{Y}}{\rho_t v_i^2} \right)^{\frac{2+\mu}{2}} \right]^{-\frac{3\mu}{2+\mu}}, \quad (6)$$

where m_i is the impactor mass, ρ_t is the target density, g is the surface gravity, a is the impactor radius, v_i is the impactor velocity, ρ_i is the impactor density, \bar{Y} is the target effective strength, and K_1 and μ are experimentally measured target properties. The quantities inside the brackets are the gravity-scaled size $((ga/v_i^2) (\rho_t/\rho_i)^{-1/3})$ and scaled strength $((\bar{Y} / (\rho_t v_i^2))^{\frac{2+\mu}{2}})$. The residence of a crater within the strength or gravity regimes depends upon which of the two terms dominates.

[47] For the specific case of secondary craters, we assume that $\rho_t = \rho_i$, because the impactor is a flying chunk of the target surface. Equation (6) then simplifies to:

$$V = K_1 \left(\frac{m_i}{\rho_t} \right) \left[\left(\frac{ga}{v_i^2} \right) + \left(\frac{\bar{Y}}{\rho_t v_i^2} \right)^{\frac{2+\mu}{2}} \right]^{-\frac{3\mu}{2+\mu}}. \quad (7)$$

We can use secondaries as a lower limit constraint on cratering strength if we compare the relative magnitude between the gravity-scaled size and the scaled strength. The fragments that create secondaries follow an inverse mass-velocity relationship, such that the fastest moving ejecta are the smallest fragments. Indeed, the size of the fragments falls off rapidly enough that the increase in velocity does not create larger craters, i.e., the average diameter of distant secondaries decreases despite the higher impact velocity that formed them.

[48] Tyre (Figure 5) is the largest primary impact crater on Europa, and created adjacent secondaries larger than 2 km (Figure 6), large enough that they formed in the gravity regime. (See sections 5.1 and 5.2. Basically, the StC transition occurs at larger diameters than the StG transition, and because the StC transition on Europa starts to occur at 2 km, anything larger than 2 km is above *both* the StG and the StC transitions.) Figure 7 illustrates that the more distant secondaries (within the adjacent field) are smaller, even though the fragments that formed them impacted at higher speeds. The same inverse size-velocity relationship holds at all distances. The minimum speed at which secondaries form around Tyre is no more than a few hundred m/s, while the maximum speed is set by Europa’s escape speed, roughly 2 km/s. However, because of the inverse relationship between ejection velocity and fragment size, it is possible that the Tyre fragments ejected at the maximum secondary-formation

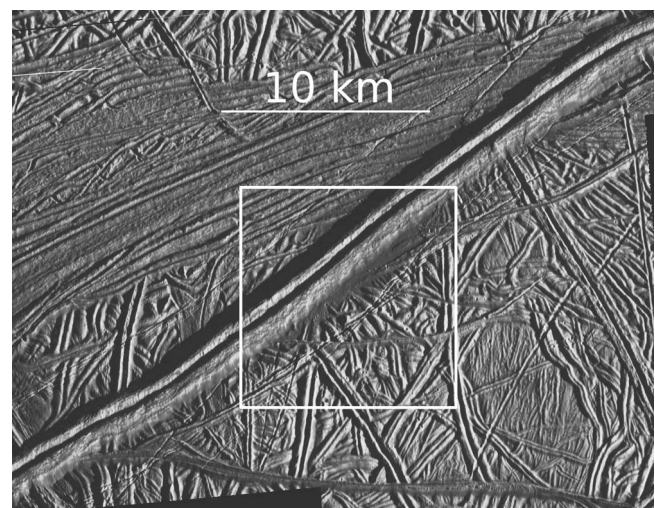


Figure 10. Portion of Galileo image sequence E06BRTPLN02. A shotgun blast of secondary craters from Pwyll transects the double ridge in this mosaic. The secondaries ejected and liberated material from the double ridge that accumulated at the base, creating a dark blanket of material that is easily distinguished from the downslope material seen elsewhere along the ridge. The white box outlines the region seen in Figure 11.

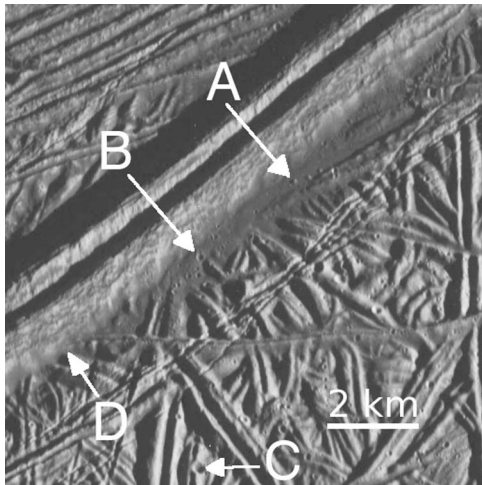


Figure 11. The portion of Galileo image sequence E06BRTPLN02 outlined in Figure 10. Numerous small secondaries from Pwyll are scattered throughout the ridged plains, up to the flank of the large double ridge. Rather than forming craters on the ridge, the impacting fragments eroded the ridge, leaving a dark blanket of material at the ridge base. Arrow A indicates one of several positive-relief “boulders” that may have fallen from the ridge. Arrow B points to one of several secondaries large enough to remain visible at the ridge-flank bottom. Arrow C points to a crater whose left-hand rim partly formed by excavating a small ridge (compare with the crater in Figure 9d). At arrow D, the contact between the double ridge and adjacent terrain has no secondaries and is distinct from the contact between arrows A and B (with secondaries).

speed (2 km/s) were small enough that they formed secondary craters in the strength regime. This is not unreasonable because examination by *Bierhaus et al.* [2001] of high-resolution Galileo images (about 10 m/pix) found that the ~25 km primary crater Pwyll generated hundreds of small secondaries, tens of meters in diameter, at a location roughly 1000 km distant from Pwyll. Secondaries were visible to the limit of the image resolution suggesting yet smaller craters exist. Tyre must also generate such a population of secondaries. (Indeed, *Bierhaus et al.* [2005] find secondaries in all high-resolution Europa images, and though it is challenging to associate the parent crater in most cases, presumably the largest primaries broadcast the largest population of secondaries.)

[49] By finding the scaled strength that permits the slow-moving Tyre secondaries to form in the gravity regime, and the fastest moving Tyre secondaries to form in the strength regime, we can estimate the minimum strength.

[50] To that end, we use the spall diameter-velocity relationship from *McEwen and Bierhaus* [2006]:

$$D_{\text{spall}} = a_p \left(\frac{v_{\text{spall}}}{1.5} \right)^{-1.2}, \quad (8)$$

where D_{spall} is the spall diameter, a_p is the primary impactor radius, and v_{spall} is the ejection and impact velocity of the fragment. Substituting $D_{\text{spall}}/2$ for a in the scaled gravity

size (ga/v_i^2), and assigning $v_{\text{spall}} = v_i$ in the scaled gravity size term gives

$$\frac{ga}{v_i^2} = \frac{ga_p}{2v_i^2} \left(\frac{v_i}{1.5} \right)^{-1.2}. \quad (9)$$

Figure 8 plots the scaled gravity size derived above for Tyre secondaries (gray line) and several curves of scaled strength for different values of \bar{Y} . The gray line assumes a 2 km impactor formed Tyre, which we derived following the formulation of *Zahnle et al.* [2003]. The scaled strength curves assume $\mu = 0.55$ [*Holsapple*, 1993] and ice strengths of 17 MPa [*Lange and Ahrens*, 1987], 1.9 MPa [*Burchell et al.*, 2005], 0.2 MPa (the approximate lower limit value from the StC transition, calculated above), and 0.05 MPa, which is approximately the \bar{Y} value that allows the large, adjacent Tyre secondaries to form in the gravity regime, and the distant Tyre secondaries to form in the strength regime. This is a minimum value, since all Tyre secondaries, including the distant ones, may form in the gravity regime. Note that the vertical location of the gray curve, and thus the minimum strength, depends on the value of a_p , which we do not know exactly. The uncertainty in a_p is at least tens of percent, and may be a factor of two. However, we emphasize that the intent of this calculation is to set a lower bound on the cratering strength.

5.4. Discussion

[51] Though the effective strength (currently) does not have a quantitative relationship to traditional measures of strength (e.g., compressive, shear or tensile strengths), we can make some analysis by analogy. Estimates of the effective strength of rocky surfaces (Mars at 9–12 MPa [*Stewart and Valiant*, 2006]) are at the low end (10–90 MPa [*Schultz*, 1995]) of compressive strength for a basaltic rock mass that incorporate the weakening effects of scale. *Holsapple* [1993] lists the effective strength for common terrestrial geologic materials: dry soil is 0.18 MPa, wet soil is 1.14 MPa, soft rock is 7.6 MPa, and hard rock is 18 MPa.

[52] If we assign the same general relationship between the effective strength in ice and a physically measurable strength value, then Europa's ice strength could approach the lab-reported values of, for example, ~1.2 MPa for tensile

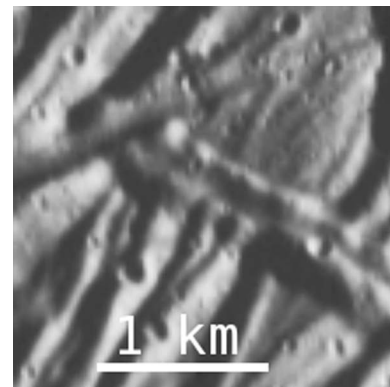


Figure 12. Highly magnified portion of Galileo image sequence E06BRTPLN02. The small secondaries are from Pwyll, over 1000 km to the south. The diameter of the secondaries are similar to the ridge width.

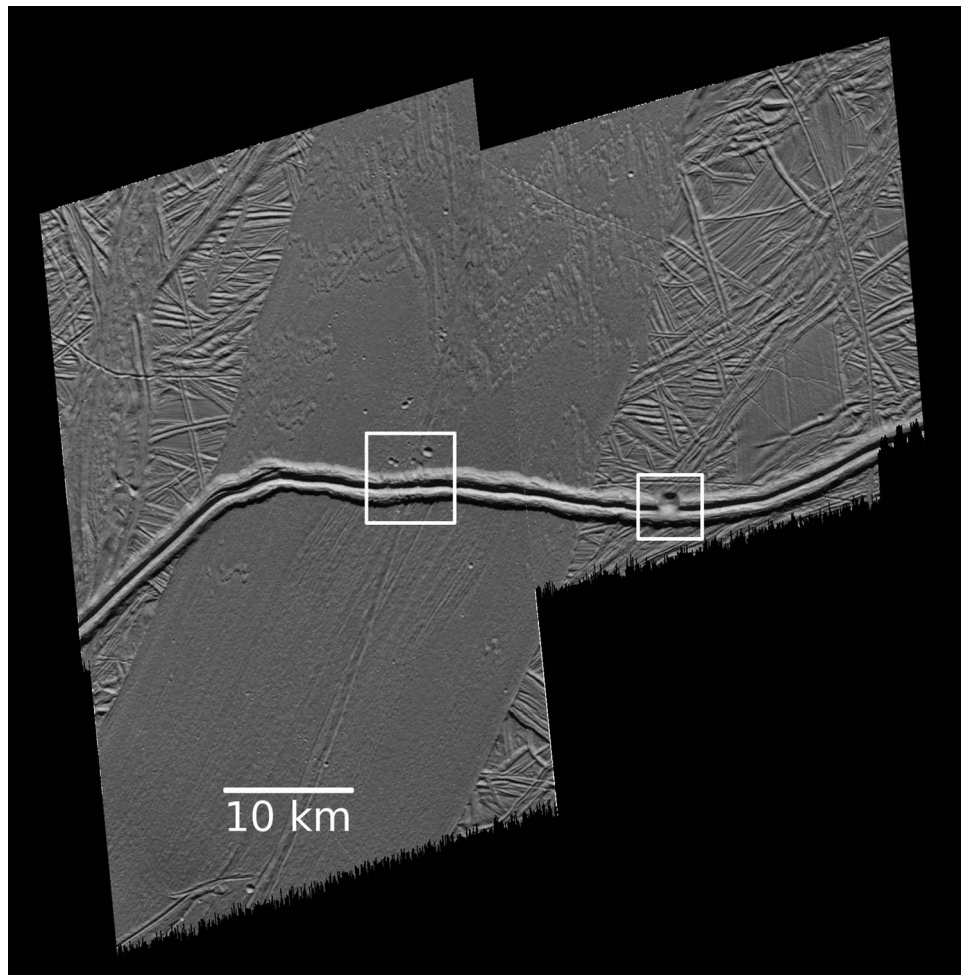


Figure 13. Galileo image sequence E17THYLIN01. Both primary and secondary craters hit the prominent double ridge. The box in the center outlines the region in Figure 14 (a cluster of secondaries); the box on the right outlines the primary crater seen in Figure 9d.

strength [Schulson, 1999]. Consequently, our minimum value of the effective strength (0.05 MPa, estimated from observations of Tyre secondaries), though similar to the strength required by the cycloid-formation models (less than 0.05 MPa tensile strength), likely reflects a surface tensile strength that is factors of several larger.

[53] Our observation that the d/D of European secondaries follows two major traits of secondaries on rocky surfaces suggests that the subsurface depths that the secondaries probe – from tens of meters to several hundred meters – respond to cratering in a similar fashion to rocky regoliths.

6. Ridge Response to Cratering

[54] Observations of craters on ridges provide additional, albeit currently qualitative, constraints on the internal structure of ridges. While there are multitudes of ridges and small craters that formed on ridges, few examples are seen at sufficient resolution to enable thoughtful examination. We present some cases here.

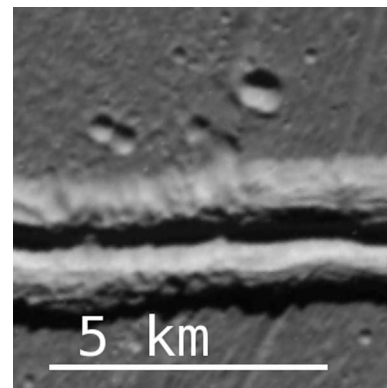


Figure 14. Portion of Galileo image sequence E17THYLIN01. A cluster of secondary craters whose formation partially eroded a double ridge. Individual craters did not form on the ridge top or flanks, rather, as is the case in Figure 11, the craters excavated and liberated material that subsequently moved downslope.

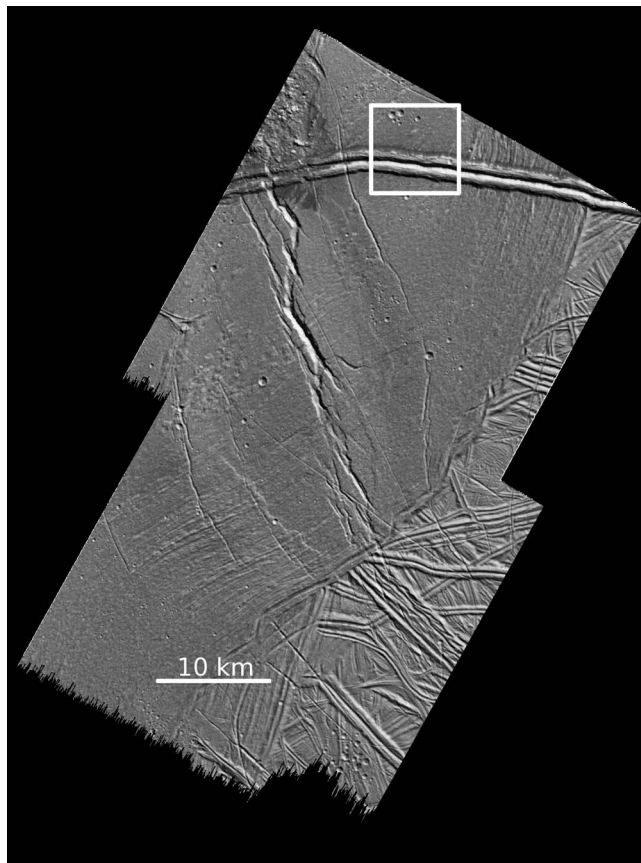


Figure 15. Galileo image sequence E17LIBLIN01. Clusters of secondaries appear throughout this mosaic. The boxed region is shown in Figure 16.

6.1. Primary Impacts

[55] Figure 9 shows the craters used for this discussion. Figures 9b and 9d are images of small primary craters that formed on ridges. At the image resolution limit in Figure 9b, there is no evidence that the preexisting ridges controlled the shape of the crater rim or cavity, even though the width of the double ridge is 0.48 km, or $>1/3$ the crater diameter. In D, the ridge superimposed by the crater is almost the same size as the crater diameter and the ridge significantly contributed to the crater morphology. One section of the crater wall appears to have formed by displacing ridge material into the double-ridge trough and even onto the adjacent ridge. The subtle structure on the crater floor could be downslope material, or represent a more competent “basement” that was resistant to excavation. With the exception of the crater seen in D, the ridges do not seem to impose a noticeable non-circular signal on the outline of the crater rims. Contrast this observation with analysis of Meteor Crater [Shoemaker, 1963] showing how subsurface structure can control the outline of a small crater on Earth.

6.2. Secondary Impacts

[56] Figure 10 shows a portion of the ~ 20 m/pix E06BRTPLN02 sequence. A swath of secondary craters from Pwyll (a 26 km crater over 1000 km distant from this region) transects the ridge; the craters are not visible at this

magnification. However, at the location of the transect (white box), the secondaries caused a noticeable increase in downslope debris at the contact margin between the prominent double-ridge and the underlying ridged plains. The white box is also the outline of the region in Figure 11 (a magnified portion of which appears in Figure 12), which clearly shows numerous secondaries in the surrounding ridged plains. There are several positive relief features, which could be ice boulders liberated from the ridge flank by the impacting fragments.

[57] Figure 13 is the ~ 44 m/pix E17THYLIN01 mosaic. A large double ridge crosses background ridged plains and a “wide band”. Superimposed on the double ridge is a secondary cluster (left white box). The source primary is currently undetermined, though could be the ~ 36 km Taliesin. Also superimposed on the double ridge is the primary seen in Figure 9d (right white box). Figure 14 is the region outlined in the left box. Though lower resolution than Figure 11, the ridge clearly expresses ballistic erosion from the impacting fragments, and individual secondary craters are hard to distinguish on the ridge.

[58] Contrast those examples with Figures 15 and 16, which show a cluster of secondaries that formed near, but not on, a double ridge. Two small craters (arrowed in Figure 16) appear on top of the ridge. Both are spatially distinct and do not modify the ridge beyond their crater cavities.

[59] Individual secondaries that form near or on the top of a ridge do not deliver enough energy to disrupt the ridge or cause damage beyond the excavated volume of the crater. However, the essentially simultaneous delivery of multiple fragments onto a ridge deposits sufficient energy to cause disruption of ridge morphology. Though the energy is distributed in multiple low-energy impacts, the crater cavities are excavating into material that is weakened by an adjacent impact. On flat surfaces these interactions are radiated into an effectively infinite subsurface, but on small topographical features such as a ridge, the expanding shock waves of multiple small impacts can interact with multiple sloped free

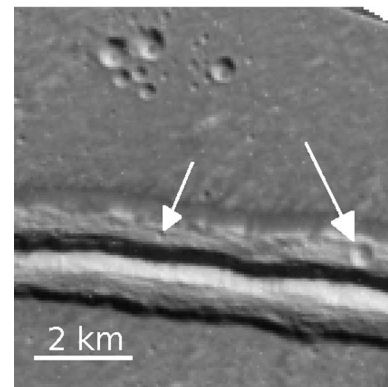


Figure 16. Portion of Galileo image sequence E17LIBLIN01. Unlike Figures 11 and 14, a cluster of secondary craters formed near, but not on, a double ridge. Individual fragments, which may or may not be a part of the same secondary event, struck the ridge top, making two craters (arrowed). Even the larger of the two craters, whose diameter is nearly equivalent to the ridge top width, did not disrupt the ridge morphology beyond the crater rim.

surfaces (e.g., ridge top and flanks). We believe these interactions allow clusters of secondaries to disrupt ridges where individual an secondary could not.

[60] Figure 12 is a highly magnified portion of the ~20 m/pix E06BRTPLN02 sequence, showing Pwyll secondaries that formed on small ridges, with sizes comparable to the diameters of the secondaries. The appearance of the secondaries suggests the crater cavities primarily formed by displacing material, rather than by excavated and ejecting material.

6.3. Implications for Ridge and Surface Properties

[61] Primary craters generate sufficient peak pressures and particle velocities in the surface that the ridges are removed topographically, and the ridges do not seem to control or modify the typical circular outline of the craters. (Except in the one case in which a small primary was approximately the scale of the ridge in which it formed.) An individual secondary impact that forms a distinct crater does little to affect the integrity of a ridge, while a cluster of near-simultaneous secondary impacts cause ballistic erosion. The Pwyll secondaries seen in Figures 10–12 formed from fragments impacting at about 1 km/s, creating a peak pressure of 0.79 GPa. Distinct craters formed on sufficiently small ridges, but the large double ridge (one ridge of the double ridge is from 0.7 km to 1.0 km across) sustained minor damage. This implies that the magnitude of the decayed shock wave of the secondary impacts was too small at the ridge edges to create serious disruption, but the multiple small impacts generated obvious mass wasting.

7. Summary and Conclusions

[62] We use topography derived from stereo and photogrammetry of high-resolution Galileo images to study the morphology and d/D values of small primary craters and secondary craters. For small primaries we observe a d/D of 0.17, which is close to the 0.2 mean value observed on other planetary surfaces. The difference may simply be due to the uncertainty in the measurement, though there is some chance the observation is real. For secondaries, the data reveal two trends: (1) on average, all secondaries have a shallow d/D relative to primaries (which is a trend seen on other crater surfaces); and (2) the d/D ratio of secondaries tends to increase with increasing distance from the parent primary crater, likely due to the higher velocities of the impacts.

[63] We use our observations of the craters to provide constraints on the properties of Europa's surface and near surface. We use the primary crater transition diameter for simple-to-complex morphologies to estimate an effective strength between 0.19 and 0.36 MPa. We use observations of Tyre secondaries to set a lower limit on the effective strength of 0.05 MPa.

[64] Because derived effective strengths from rocky surfaces tend to be lower than typical strength measures of those same materials, we expect the same to be true of Europa. Consequently, our minimum value of the effective strength (0.05 MPa, estimated from observations of Tyre secondaries), though similar to the strength required by the cycloid-formation models (less than 0.05 MPa tensile strength), likely reflects a surface tensile strength that is

factors of several larger. The d/D behavior of the secondaries indicates that any ductile component of Europa's ice must be deeper than several hundred meters.

[65] **Acknowledgments.** We are grateful to NASA's Outer Planets Research program, which funded this work. We thank Olivier Bamouin-Jha and an anonymous reviewer for careful and thoughtful reviews of the manuscript, and Sarah Stewart-Mukhopadhyay and Francis Nimmo for helpful discussions.

References

- Arakawa, M., and N. Maeno (1997), Mechanical strength of polycrystalline ice under uniaxial compression, *Cold Reg. Sci. Technol.*, 26, 215–229, doi:10.1016/S0165-232X(97)00018-9.
- Bierhaus, E. B., C. R. Chapman, W. J. Merline, S. M. Brooks, and E. Asphaug (2001), Pwyll secondaries and other small craters on Europa, *Icarus*, 153, 264–276, doi:10.1006/icar.2001.6690.
- Bierhaus, E. B., C. R. Chapman, and W. J. Merline (2005), Secondary craters on Europa and implications for cratered surfaces, *Nature*, 437, 1125–1127, doi:10.1038/nature04069.
- Bierhaus, E. B., K. J. Zahnle, and C. R. Chapman (2009), *Europa*, 161 pp., Univ. of Arizona Press, Tucson, Ariz.
- Black, G. J., D. B. Campbell, and P. D. Nicholson (2001a), Icy Galilean satellites: Modeling radar reflectivities as a coherent backscatter effect, *Icarus*, 151, 167–180, doi:10.1006/icar.2001.6616.
- Black, G. J., D. B. Campbell, and S. J. Ostro (2001b), Icy Galilean satellites: 70 cm radar results from Arecibo, *Icarus*, 151, 160–166, doi:10.1006/icar.2001.6615.
- Burchell, M. J., J. Leliwa-Kopystyński, and M. Arakawa (2005), Cratering of icy targets by different impactors: Laboratory experiments and implications for cratering in the Solar System, *Icarus*, 179, 274–288, doi:10.1016/j.icarus.2005.06.010.
- Chapman, C. R., and W. B. McKinnon (1986), Cratering of planetary satellites, in *Satellites*, edited by J. A. Burns and M. S. Matthews, pp. 492–580, Univ. of Ariz. Press, Tucson.
- Durham, W. B., and L. A. Stern (2001), Rheological properties of water ice—Applications to satellites of the outer planets, *Annu. Rev. Earth Planet. Sci.*, 29, 295–330, doi:10.1146/annurev.earth.29.1.295.
- Efford, N. D. (1991), Sources of error in the photogrammetric determination of planetary topography—A reappraisal, *Earth Moon Planets*, 54, 19–58, doi:10.1007/BF00055046.
- Eluszkiewicz, J. (2004), Assessing porosity structure in Europa's crust, paper presented at Workshop on Europa's Icy Shell: Past, Present, and Future, Lunar Planet. Inst., Houston, Tex.
- Figueredo, P. H., and R. Greeley (2004), Resurfacing history of Europa from pole-to-pole geologimapping, *Icarus*, 167, 287–312, doi:10.1016/j.icarus.2003.09.016.
- Gault, D. E., and E. D. Heitowitz (1963), The partition of energy for hypervelocity impact craters formed in rock, in *Proceedings of the 6th Hypervelocity Impact Symposium*, pp. 420–456, Def. Doc. Cent. for Sci. and Tech. Inf., Alexandria, Va.
- Holsapple, K. A. (1993), The scaling of impact processes in planetary sciences, *Annu. Rev. Earth Planet. Sci.*, 21, 333–373, doi:10.1146/annurev.earth.21.050193.002001.
- Holsapple, K. A., and K. R. Housen (2007), A crater and its ejecta: An interpretation of Deep Impact, *Icarus*, 187, 345–356, doi:10.1016/j.icarus.2006.08.029.
- Hoppa, G. V., B. Randall Tufts, R. Greenberg, T. A. Hurford, D. P. O'Brien, and P. E. Geissler (2001), Europa's rate of rotation derived from the tectonic sequence in the Astypalaea Region, *Icarus*, 153, 208–213, doi:10.1006/icar.2001.6663.
- Housen, K. R., and K. A. Holsapple (2003), Impact cratering on porous asteroids, *Icarus*, 163(1), 102–119, doi:10.1016/S0019-1035(03)00024-1.
- Jankowski, D. G., and S. W. Squyres (1991), Sources of error in planetary photogrammetry, *J. Geophys. Res.*, 96(E4), 20,907–20,922, doi:10.1029/91JE02209.
- Kato, M., Y. Iijima, M. Arakawa, Y. Okimura, A. Fujimura, N. Maeno, and H. Mizutani (1995), Ice-on-ice impact experiments, *Icarus*, 113, 423–441, doi:10.1006/icar.1995.1032.
- Lange, M. A., and T. J. Ahrens (1987), Impact experiments in low-temperature ice, *Icarus*, 69, 506–518, doi:10.1016/0019-1035(87)90020-0.
- McEwen, A. S. (1986), Exogenic and endogenic albedo and color patterns on Europa, *J. Geophys. Res.*, 91(B8), 8077–8097, doi:10.1029/JB091iB08p08077.

- McEwen, A. S. (1990), Global color and albedo variations on Triton, *Geophys. Res. Lett.*, *17*(10), 1765–1768, doi:10.1029/GL017i010p01765.
- McEwen, A. S. (1991), Photometric functions for photoclinometry and other applications, *Icarus*, *92*, 298–311, doi:10.1016/0019-1035(91)90053-V.
- McEwen, A. S., and E. B. Bierhaus (2006), The importance of secondary cratering to age constraints on planetary surfaces, *Annu. Rev. Earth Planet. Sci.*, *34*, 535–567, doi:10.1146/annurev.earth.34.031405.125018PDF.
- McKinnon, W. B., and P. M. Schenk (1995), Estimates of comet fragment masses from impact crater chains on Callisto and Ganymede, *Geophys. Res. Lett.*, *22*(13), 1829–1832, doi:10.1029/95GL01422.
- Melosh, H. J. (1989), *Impact Cratering: A Geologic Process*, 45 pp., NASA, New York.
- Michalski, J. R., and R. Greeley (2002), En echelon ridge and trough structures on Europa, *Geophys. Res. Lett.*, *29*(10), 1498, doi:10.1029/2002GL014956.
- Moore, J. M., et al. (1998), Large impact features on Europa: Results of the Galileo nominal mission, *Icarus*, *135*, 127–145, doi:10.1006/icar.1998.5973.
- Moore, J. M., et al. (2001), Impact features on Europa: Results of the Galileo Europa mission (GEM), *Icarus*, *151*, 93–111, doi:10.1006/icar.2000.6558.
- Nolan, M. C., E. Asphaug, H. J. Melosh, and R. Greenberg (1996), Impact craters on asteroids: Does gravity or strength control their size?, *Icarus*, *124*, 359–371, doi:10.1006/icar.1996.0214.
- Oberbeck, V. R., and R. H. Morrison (1973), The secondary crater herringbone pattern, *Lunar Planet. Inst. Tech. Rep.*, *4*, 570.
- O'Keefe, J. D., and T. J. Ahrens (1993), Planetary cratering mechanics, *J. Geophys. Res.*, *98*(E9), 17,011–17,028, doi:10.1029/93JE01330.
- Pike, R. J. (1977), Apparent depth/apparent diameter relation for lunar craters, *Lunar Planet. Sci.*, *8*, 3427–3436.
- Pike, R. J. (1980), Formation of complex impact craters—Evidence from Mars and other planets, *Icarus*, *43*, 1–19, doi:10.1016/0019-1035(80)90083-4.
- Pike, R. J., and D. E. Wilhelms (1978), Secondary impact craters on the Moon: Topographic form and geologic process, *Lunar Planet. Inst. Tech. Rep.*, *9*, 907–909.
- Richardson, J. E., H. J. Melosh, C. M. Lisse, and B. Carcich (2007), A ballistics analysis of the Deep Impact ejecta plume: Determining Comet Tempel 1's gravity, mass, and density, *Icarus*, *191*, 176–209, doi:10.1016/j.icarus.2007.08.033.
- Sarid, A. R., R. Greenberg, G. V. Hoppa, T. A. Hurford, B. R. Tufts, and P. Geissler (2002), Polar wander and surface convergence of Europa's ice shell: Evidence from a survey of strike-slip displacement, *Icarus*, *158*(1), 24–41, doi:10.1006/icar.2002.6873.
- Schenk, P. M. (1991), Ganymede and Callisto—Complex crater formation and planetary crusts, *J. Geophys. Res.*, *96*(E1), 15,635–15,664, doi:10.1029/91JE00932.
- Schenk, P. M. (2002), Thickness constraints on the icy shells of the Galilean satellites from a comparison of crater shapes, *Nature*, *417*(6887), 419–421, doi:10.1038/417419a.
- Schenk, P. M. (2009), Slope characteristics of Europa: Constraints for landers and radar sounding, *Geophys. Res. Lett.*, *36*, L15204, doi:10.1029/2009GL039062.
- Schenk, P. M., and D. B. J. Bussey (2004), Galileo stereo topography of the lunar north polar region, *Geophys. Res. Lett.*, *31*, L23701, doi:10.1029/2004GL021197.
- Schenk, P. M., and R. T. Pappalardo (2004), Topographic variations in chaos on Europa: Implications for diapiric formation, *Geophys. Res. Lett.*, *31*, L16703, doi:10.1029/2004GL019978.
- Schenk, P., and E. Turtle (2009), *Europa*, 181 pp., Univ. of Ariz. Press, Tucson.
- Schenk, P. M., C. R. Chapman, K. Zahnle, and J. M. Moore (2004), Ages and interiors: The cratering record of the Galilean satellites, in *Jupiter: The Planet, Satellites and Magnetosphere*, edited by F. Bagenal, T. E. Dowling and W. B. McKinnon, pp. 427–456, Cambridge Univ. Press, Cambridge, U. K.
- Schulson, E. M. (1999), The structure and mechanical behavior of ice, *JOM*, *51*, 21–27, doi:10.1007/s11837-999-0206-4.
- Schultz, P. H., and D. E. Gault (1985), Clustered impacts—Experiments and implications, *J. Geophys. Res.*, *90*(B5), 3701–3732, doi:10.1029/JB090iB05p03701.
- Schultz, R. A. (1995), Limits on strength and deformation properties of jointed basaltic rock masses, *Rock Mech. Rock Eng.*, *28*, 1–15, doi:10.1007/BF01024770.
- Senft, L. E., and S. T. Stewart (2007), Modeling impact cratering in layered surfaces, *J. Geophys. Res.*, *112*, E11002, doi:10.1029/2007JE002894.
- Shoemaker, E. M. (1963), *Impact Mechanics at Meteor Crater, Arizona*, 301 pp., Univ. of Chicago Press, Chicago, Ill.
- Spaun, N. A., R. T. Pappalardo, and J. W. Head (2003), Evidence for shear failure in forming near-equatorial lineae on Europa, *J. Geophys. Res.*, *108*(E6), 5060, doi:10.1029/2001JE001499.
- Spencer, J. R. (1987), Icy Galilean satellite reflectance spectra—Less ice on Ganymede and Callisto?, *Icarus*, *70*, 99–110, doi:10.1016/0019-1035(87)90077-7.
- Spencer, J. R., L. K. Tamppari, T. Z. Martin, and L. D. Travis (1999), Temperatures on Europa from Galileo PPR: Nighttime thermal anomalies, *Science*, *284*, 1514–1516, doi:10.1126/science.284.5419.1514.
- Stewart, S. T., and T. J. Ahrens (2005), Shock properties of H₂O ice, *J. Geophys. Res.*, *110*, E03005, doi:10.1029/2004JE002305.
- Stewart, S. T., and G. J. Valiant (2006), Martian subsurface properties and crater formation processes inferred from fresh impact crater geometries, *Meteorol. Planet. Sci.*, *41*, 1509–1537, doi:10.1111/j.1945-5100.2006.tb00433.x.
- Turtle, E. P., and B. A. Ivanov (2002), Numerical simulations of impact crater excavation and collapse on Europa: Implications for ice thickness, *Lunar Planet. Inst. Conf.*, *33rd*, Abstract 1431.
- Turtle, E. P., and E. Pierazzo (2001), Thickness of a European ice shell from impact crater simulations, *Science*, *294*, 1326–1328, doi:10.1126/science.1062492.
- Zahnle, K., L. Dones, and H. F. Levison (1998), Cratering rates on the Galilean satellites, *Icarus*, *136*, 202–222, doi:10.1006/icar.1998.6015.
- Zahnle, K., P. Schenk, H. Levison, and L. Dones (2003), Cratering rates in the outer Solar System, *Icarus*, *163*(2), 263–289, doi:10.1016/S0019-1035(03)00048-4.
- Zahnle, K., J. L. Alvarillos, A. Dobrovolskis, and P. Hamill (2008), Secondary and sesquinary craters on Europa, *Icarus*, *194*, 660–674, doi:10.1016/j.icarus.2007.10.024.

E. B. Bierhaus, Space Systems Company, Lockheed Martin, MS S8110, PO Box 179, Denver, CO 80201, USA. (edward.b.bierhaus@lmco.com)
 P. M. Schenk, Lunar and Planetary Institute, 3600 Bay Area Blvd., Houston, TX 77058, USA.